Geophysical Journal International

Geophys. J. Int. (2025) **243,** 1–15
Advance Access publication 2025 October 1
Research Paper

https://doi.org/10.1093/gji/ggaf387

Recursive interferometric surface-wave suppression for improved reflection imaging

Faezeh Shirmohammadi [*], Deyan Draganov, Ranajit Ghose, Eric Verschuur, Jan Thorbecke and Kees Wapenaar

Department of Geoscience and Engineering, Delft University of Technology, 2628 *CN Delft, the Netherlands. E-mail: D.S.Draganov@tudelft.nl*

Accepted 2025 September 26. Received 2025 September 5; in original form 2025 February 20

SUMMARY

High-resolution seismic reflections are essential for imaging and monitoring applications. In seismic land surveys using sources and receivers at the surface, surface waves often dominate, masking the reflections. In this study, we demonstrate the efficacy of a two-step procedure to suppress surface waves in an active-source reflection seismic data set. First, we apply seismic interferometry (SI) by cross-correlation, turning receivers into virtual sources to estimate the dominant surface waves. Then, we perform adaptive subtraction to minimize the difference between the surface waves in the original data and the result of SI. We propose a new approach where the initial suppression results are used for further iterations, followed by adaptive subtraction. This technique aims to enhance the efficacy of data-driven surface-wave suppression through an iterative process. We use a 2-D seismic reflection data set from Scheemda, situated in the Groningen province of the Netherlands, to illustrate the technique's efficiency. A comparison between the data after recursive interferometric surface-wave suppression and the original data across time and frequency–wavenumber domains shows significant suppression of the surface waves, enhancing visualization of the reflections for subsequent subsurface imaging and monitoring studies.

Key words: Seismic interferometry; Seismic noise; Surface waves and free oscillations; Wave propagation.

1 INTRODUCTION

Seismic data acquired on land are often contaminated by surface waves, which are a significant noise source for reflection seismic studies. The surface waves can have a frequency content similar to that of the targeted reflections; since the velocities of the surface waves are lower but close to the velocities of the *S* wave, the asymptotes of the *S*-wave reflection hyperbolae have slopes very similar to those of the surface waves. Both these factors make it challenging to suppress the surface waves from such a data set. Conventionally, surface waves are suppressed during data processing using methods such as frequency-offset (f-x) (Öz Yilmaz 2001), frequency–wavenumber (f-k) or bandpass filtering. However, these approaches can prove ineffective when surface waves are scattered and overlap with the frequency and moveout of the reflected body waves that we intend to preserve. The f-k filter may result in artefacts due to signal distortion and spatial correlation of the background noise because the surface-wave energy may be distributed over a significant range of the f-k spectrum (Konstantaki *et al.* 2015), thus further lowering the quality of the reflections.

Recently, the prediction of surface waves with seismic interferometry (SI) and their subsequent adaptive subtraction from seismic reflection data has emerged as a technique for suppressing surface waves (Dong *et al.* 2006; Halliday *et al.* 2010). In SI, seismic observations from various receiver locations are, for example, cross-correlated to retrieve new seismic responses from virtual sources positioned at the receivers' locations (Lobkis & Weaver 2001; Campillo & Paul 2003; Curtis *et al.* 2006; van Manen *et al.* 2006; Wapenaar & Fokkema 2006). This process enables the retrieval of seismic responses between pairs of receivers. For suppression, the retrieved responses are then subtracted from the original field recordings using least-squares matching, resulting in data with suppressed surface waves. This suppression technique is usually called interferometric surface-wave suppression.

In previous studies, the interferometric surface-wave suppression was applied in a non-recursive way on the data. Halliday *et al.* (2010) demonstrated its effectiveness in the context of hydrocarbon exploration, while Konstantaki *et al.* (2015) and Liu *et al.*

[*]*Now at:* Fugro Innovation and Technology B.V., NL-2631 RT Nootdorp, the Netherlands.

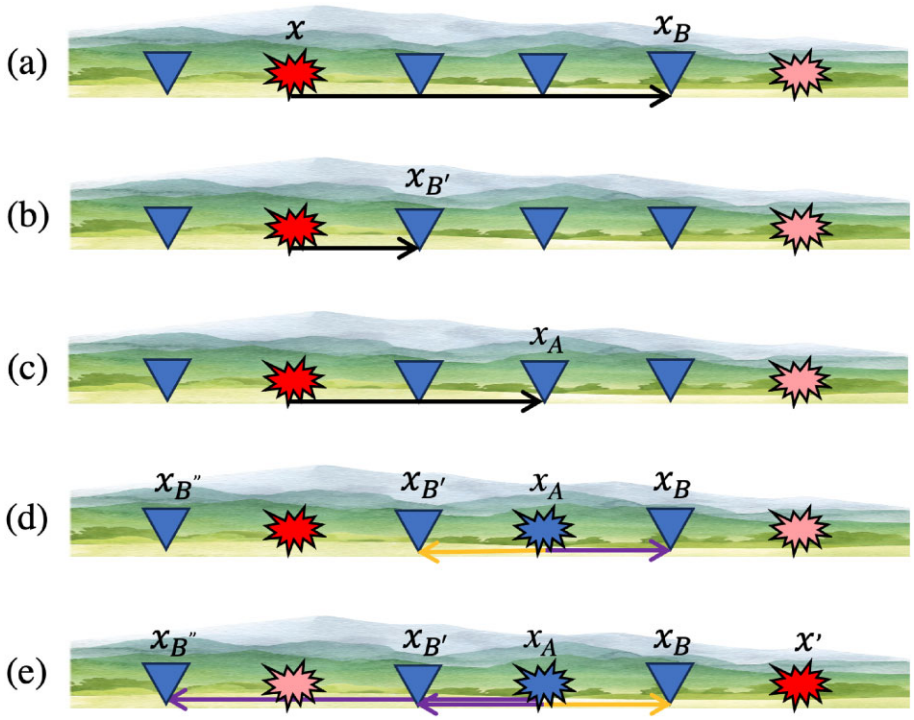

Figure 1. Schematic representation of seismic interferometry for retrieving surface waves. (a), (b) and (c) The surface wave from the active source **x** recorded at $\mathbf{x}_B$, $\mathbf{x}_{B'}$ and $\mathbf{x}_A$, respectively. (d) The results of correlating the response at $\mathbf{x}_A$ with those at other receivers, and thus turning $\mathbf{x}_A$ into a virtual source. (e) Same as (d) but for the active source at $\mathbf{x}'$. The black arrows indicate the surface waves, while the orange and purple arrows represent the results of correlation, considering the acausal and causal parts, respectively.

(2018) showcased its utility for near-surface applications. Moreover, Balestrini *et al.* (2020) demonstrated its application for deep mineral explorations. Here, we propose a new approach using the first output of the interferometric surface-wave suppression for more iterations. We term this technique 'Recursive Interferometric Surface-wave Suppression' (RISS). This technique aims to enhance the efficacy of the data-driven surface-wave suppression through an iterative procedure.

In this study, we demonstrate RISS on a 2-D reflection data set acquired in Scheemda, Groningen province, the Netherlands. By using RISS, we aim to enhance the visualization of reflections, which can provide clearer images of the subsurface structures and enhance the overall interpretation of the seismic data. Such advancements are particularly critical for Groningen, where gas production has resulted in induced seismicity since 1963 (Muntendam-Bos *et al.* 2022). We evaluate the RISS results in comparison with those from other techniques such as time muting, band-reject filtering and f-k filtering.

Below, we first present in Section 2 the methodology of RISS. This will be followed by a description of the seismic data acquisition in Section 3, the results in Section 4 and then a discussion and conclusions.

2 METHODOLOGY

In our proposed approach, SI is employed first to retrieve the dominant surface waves. The retrieved surface-wave energy is subsequently adaptively subtracted from the data set. Following this, the obtained data is utilized to iterate through these two steps, contributing to the improvement of the reflection resolution. This section outlines the implementation of RISS.

2.1 Surface-wave retrieval by seismic interferometry

SI refers to the method of retrieving new seismic responses, for example between two receivers, using most commonly cross-correlation, and the result creates a virtual source at one of the receiver locations (Larose *et al.* 2006; Schuster & Zhou 2006; Wapenaar & Fokkema 2006). In an active-source survey, this process is usually achieved by cross-correlating the recordings at two receivers and then stacking the individual virtual-source traces over all available active sources (Halliday & Curtis 2008). So, the retrieved virtual-source response between two receivers at positions $\mathbf{x}_A$ and $\mathbf{x}_B$ can be expressed in the time domain in its simplest form as

$$G(\mathbf{x}_B, \mathbf{x}_A, t) + G(\mathbf{x}_B, \mathbf{x}_A, -t) = \sum_{n=1}^{N} G(\mathbf{x}_B, \mathbf{x}_n, t) * G(\mathbf{x}_A, \mathbf{x}_n, -t), \tag{1}$$

where $G(\mathbf{x}_B, \mathbf{x}_n, t)$ is the response of a recording at receiver $\mathbf{x}_B$ and $G(\mathbf{x}_A, \mathbf{x}_n, -t)$ is the time-reversed response of a recording at receiver $\mathbf{x}_A$, both from a source at $\mathbf{x}_n$ at the Earth's surface. The left-hand side of the equation represents the response and its time-reversal between the two receivers at $\mathbf{x}_A$ and $\mathbf{x}_B$ at the surface, implying that the receiver at $\mathbf{x}_A$ has been turned into a virtual source. N represents the total number of active sources at the surface and $*$ denotes convolution.

In a laterally homogeneous 2-D medium, sources at points in line with the receivers contribute to the retrieval of direct surface-wave arrivals since they are all in the stationary-phase region. So, the results retrieved by SI will be dominated by surface waves (Balestrini *et al.* 2020).

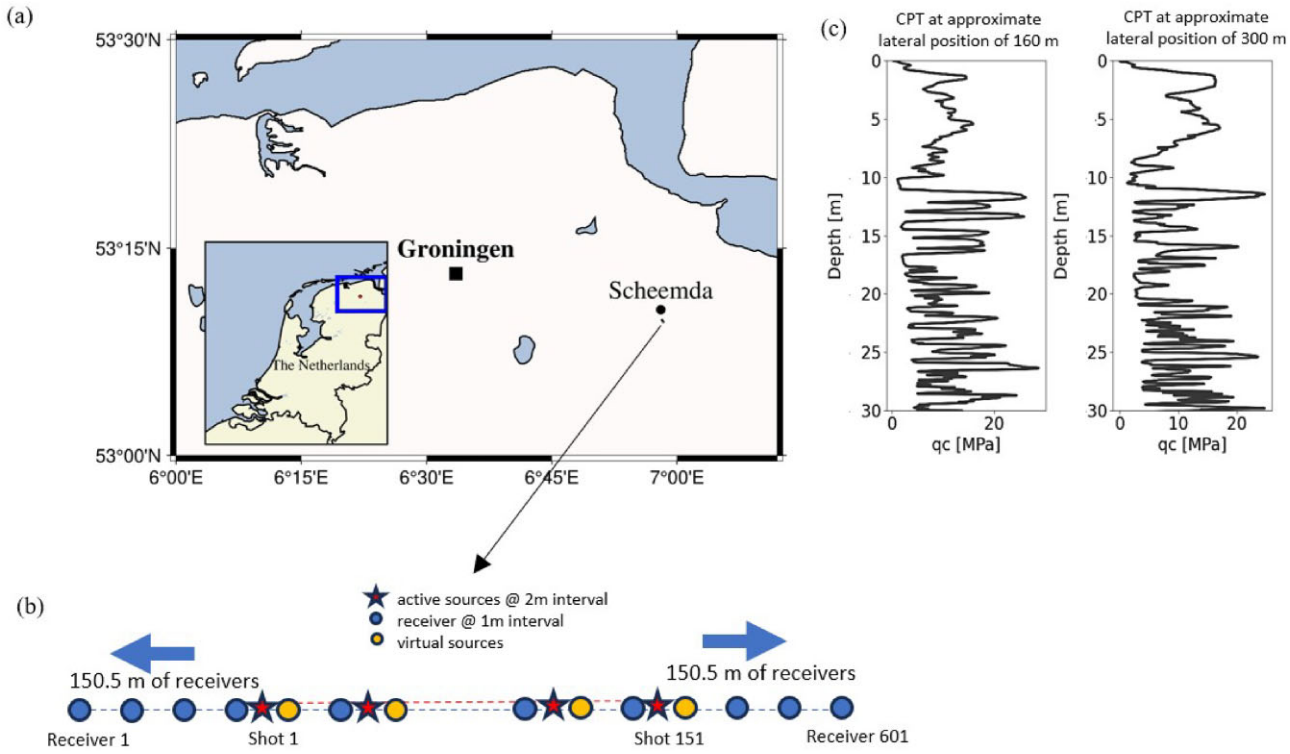

Figure 2. (a) Location of the test site, and (b) the geometry of the seismic line. The red stars represent active sources, the blue circles represent receivers and the orange circles represent receivers which act as virtual sources for applying the RISS, (c) cone-tip resistance (qc) measured at two cone penetration test (CPT) locations.

Table 1. Acquisition parameters.

Parameter	Value
Number of source positions	151
Source spacing	2 m
First source position	150.5
Last source position	450.5
Number of receiver positions per source	601
Receiver spacing	1 m
First receiver position	0 m
Frequency range of the vibrator sweep	8-250 Hz

Fig. 1 shows a schematic representation of SI for retrieving direct arrivals, including surface waves. By correlating the recording at $\mathbf{x}_B$ from the active source at $\mathbf{x}$ in Fig. 1(a) with a recording at $\mathbf{x}_A$ in Fig. 1(c), the virtual response between $\mathbf{x}_B$ and $\mathbf{x}_A$ is retrieved, as illustrated by the purple arrow in Fig. 1(d), at causal times (the causal part refers to times later than the zero time). Similarly, the virtual response between another receiver at $\mathbf{x}_{B'}$ and a receiver at $\mathbf{x}_A$ is retrieved by correlating the response at $\mathbf{x}_{B'}$ in Fig. 1(b) with that at $\mathbf{x}_A$ in Fig. 1(c), as depicted by the orange arrow in Fig. 1(d), at acausal times (the acausal part refers to times earlier than the zero time). In both cases, the receiver at $\mathbf{x}_A$ acts as a virtual source as shown by the blue explosion in Fig. 1(d). We repeat this procedure for all active sources, for example, as shown in Fig. 1(e) for another active source at $\mathbf{x}'$. Finally, the Green's function and its time-reversal between the virtual source at $\mathbf{x}_A$ and other receivers at $\mathbf{x}_B$, $\mathbf{x}_{B'}$ and $\mathbf{x}_{B''}$ are retrieved by stacking all virtual responses such as those shown in Figs 1(d) and (e).

When we want to apply this technique to a field data set, there are certain issues that need to be addressed in order to improve the resolution of the retrieved responses. First, we aim to retrieve the surface waves with SI. So, it is required that all receivers be considered on the same side of the active source, for example, for an active source at $\mathbf{x}$ in Fig. 1(a), we correlate the response for receivers $\mathbf{x}_B$ and $\mathbf{x}_{B'}$ located on the same side as the virtual source at $\mathbf{x}_A$, as shown in Figs 1(a), (b) and (c). In the same way, for an active source at $\mathbf{x}'$ in Fig. 1(e), we consider all receivers because they are on the same side as the virtual source at $\mathbf{x}_A$, as shown in Fig. 1(e). This condition is dictated by the theory of SI by cross-correlation, which states that the sources should surround the receivers, that is, there must be no sources located between the receivers involved in the correlation process.

Secondly, in the case of isotropic illumination of the receivers, a time-symmetric response between the receivers is obtained, as shown in eq. (1). Consequently, one could sum the causal and the time-reversed acausal parts of the correlated panels to improve the signal-to-noise ratio. However, in practical situations, when the illumination is not homogeneous from all sides for each pair of receivers, then parts of the response can be retrieved at acausal times and other parts at causal times. Therefore, to enhance the quality of the retrieved responses, we meticulously assess the positions of virtual source–receiver pairs and active sources. Subsequently, we opt to select either the causal or time-reversed acausal part of the correlation panel.

Considering the conditions of one-sided distribution of receivers and causality, we limit ourselves to a minimum number of traces for stacking. To maintain a high signal-to-noise ratio, we stack traces only when we have at least half the number of all active sources. We can summarize this as follows:

$$trace \begin{cases} \text{causal part, if } m > N/2 \text{ with } P_{\mathbf{x}} < P_{\mathbf{x}_A} < P_{\mathbf{x}_B}, \text{ or } P_{\mathbf{x}} > P_{\mathbf{x}_A} > P_{\mathbf{x}_B}, \text{ or } P_{\mathbf{x}_A} = P_{\mathbf{x}_B} \\ \text{time-reversed acausal, if } m > N/2 \text{ with } P_{\mathbf{x}} < P_{\mathbf{x}_B} < P_{\mathbf{x}_A}, \text{ or } P_{\mathbf{x}} > P_{\mathbf{x}_B} > P_{\mathbf{x}_A}. \end{cases}$$

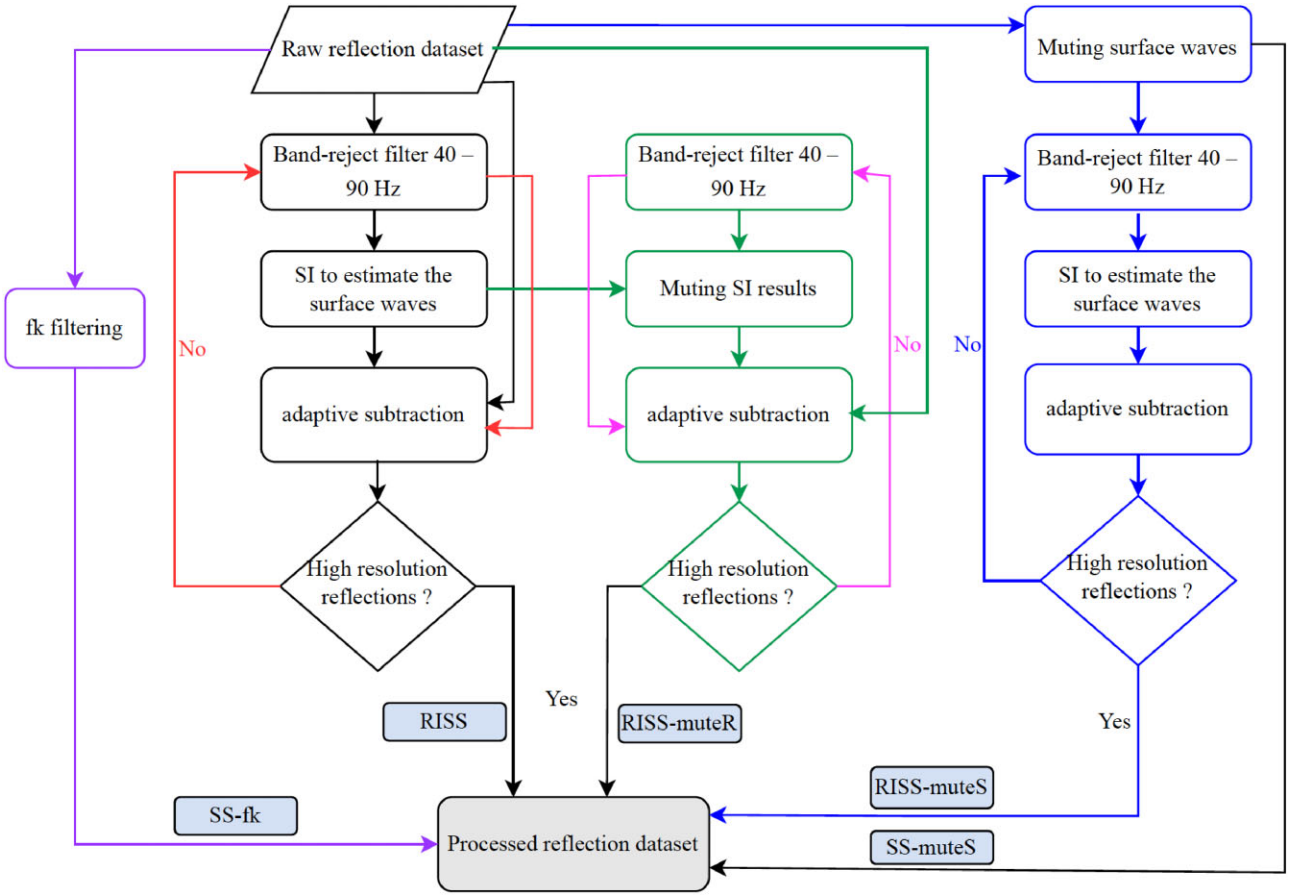

Figure 3. Flowchart for applying surface-wave suppression. RISS stands for the Recursive Interferometric Surface-wave Suppression, the RISS-muteR is same as RISS but using muted SI results, the RISS-muteS is the same as RISS but using time-muted reflection data set as input for SI, SS-fk denotes surface-wave suppression using f-k filtering, SS-muteS stands for surface-wave suppression using time-muted reflection data set.

Here, the scalar $P_{\mathbf{x}}$ is the position of active sources along a 2-D seismic line, $P_{\mathbf{x}_A}$ is the position of the virtual source, $P_{\mathbf{x}_B}$ is the position of the receiver and m is the number of active sources for stacking, which should be greater than half the total number of active sources (N). For instance, as illustrated in Fig. 1(d), for the receiver at $\mathbf{x}_{B'}$ on the left side of the virtual source at $\mathbf{x}_A$, we consider the acausal part, as indicated by the orange arrow. Similarly, for a receiver at $\mathbf{x}_B$ on the right side of the virtual source, we consider the causal part, indicated by the purple arrow. Furthermore, as depicted in Fig. 1(e), for the receiver at $\mathbf{x}_B$ on the right side of the virtual source at $\mathbf{x}_A$, we consider the acausal part, and for other receivers at $\mathbf{x}_{B'}$ and $\mathbf{x}_{B''}$, we consider the causal part, as shown by the purple arrows. Considering the above factors, we retrieve the virtual common-source gather for all receivers.

2.2 Adaptive subtraction

When each source position in an active-source survey is in close proximity to a receiver position, we are able to identify a corresponding retrieved virtual common-source gather with estimated dominant surface waves for each active source–virtual source pair. These estimates can then be adaptively subtracted from the complete responses of the active sources (Halliday & Curtis 2008; Halliday *et al.* 2010; Konstantaki *et al.* 2015). To perform adaptive subtraction, we estimate a shaping filter $\mathbf{f}$ that can minimize the following objective function (Liu *et al.* 2018; Balestrini *et al.* 2020):

$$\min_{\mathbf{f}} \|D - \mathbf{f}D_{\mathrm{SW}}\|^2, \tag{2}$$

where D stands for the field data set with surface waves and D_{SW} stands for the surface waves retrieved by SI using the field data set. The squared vertical double bars $||.||^2$ represent the L2 norm. Eq. (2) is solved using an iterative least-squares fit (Verschuur *et al.* 1992). More details can be found in Alá'i & Verschuur (2003) and Verschuur (2013). The product of estimated $\mathbf{f}$ and D_{SW} is directly subtracted from D, giving D_{ref} which represents the data after surface-wave suppression as

$$D_{\mathrm{ref}} = D - \mathbf{f}D_{\mathrm{SW}}. \tag{3}$$

The data after adaptive subtraction may still contain surface waves due to, for example, errors in estimating higher modes of surface waves. Therefore, we suggest repeating the same step of SI and adaptive subtraction but now using the output of the first adaptive subtraction as input for SI. So, we estimate surface waves from SI, and then adaptively subtract them from the output of the first iteration. Repeating these steps improves our chances of suppressing surface-wave energy, as demonstrated in the numerical example in Appendix A, thereby enhancing the resolution of reflections. We call this technique 'Recursive Interferometric Surface-wave Suppression (RISS)'. Note that RISS can be applied for one iteration or multiple iterations.

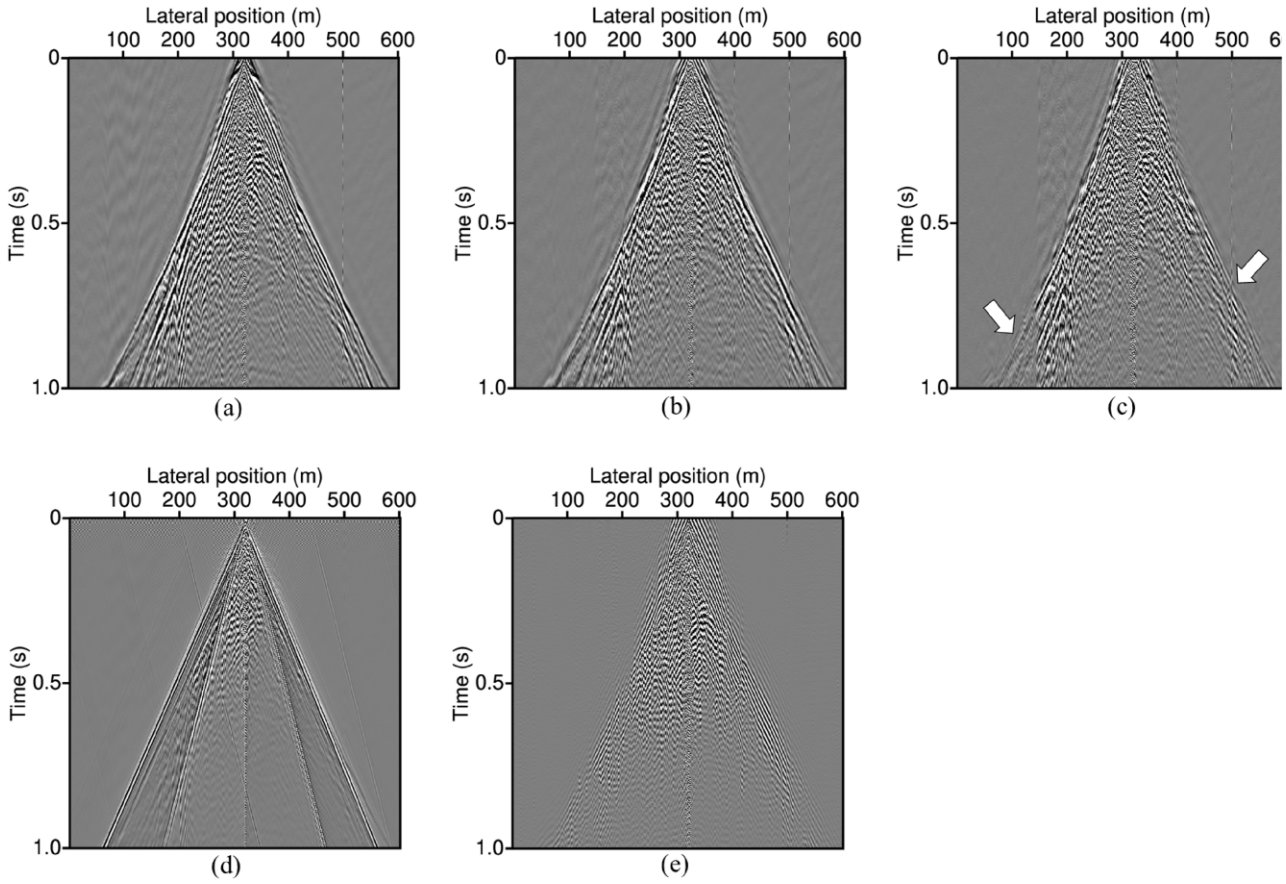

Figure 4. (a) A common-source gather for a source located at lateral position 320.5 m, (b) same common-source gather after the first iteration of the RISS, (c) same common-source gather after the second iteration of the RISS, (d) same common-source gather after fk filtering and (e) same common-source gather after band-reject filtering between 5 and 40 Hz. White arrows point to suppressed surface waves in the space-time domain.

3 SEISMIC DATA ACQUISITION

We acquired a 2-D seismic reflection data set close to the town of Scheemda in the Groningen province of the Netherlands in 2022. Figs 2(a) and (b) show the location of the site and the geometry of the reflection line, respectively. We employed an electrical linear motor system (LMS) seismic vibrator (Noorlandt *et al.* 2015) as a source, with a spacing of 2 m (red stars in Fig. 2b), and 601 three-component geophone nodes as receivers (the circles in Fig. 2b), with a spacing of 1 m. The acquisition parameters are summarized in Table 1.

For this survey, we used the electrical vibrator in the *S*-wave mode and oriented it in the cross-line direction. We then used the data recorded by the cross-line horizontal component of the geophones. Because of the orientation of the sources and the receivers, and assuming no scattering from the cross-line direction, the horizontally polarized *S* waves (*SH* waves) we record are generally decoupled from the compressional and vertically polarized *S* waves.

Fig. 2(c) illustrates two examples of cone penetrating test (CPT) data from this site, which shows that the first 30 m of this site consist of alternating layers capable of generating strong surface waves.

4 RESULTS

The primary aim of this study is to examine the effectiveness of the RISS technique. We apply the technique to common-source gathers of the field data, as introduced in Section 3. The data processing involves several steps. Fig. 3 shows a flowchart of data processing for RISS, but also other techniques such as f-k filtering and surgical muting for surface-wave suppression.

The maximum frequency in the reflected signal was less than 90 Hz. Therefore, as shown in Fig. 3, first we apply a band-reject filter between 40 and 90 Hz to all active common-source gathers to reject frequencies that primarily contain reflections but not surface waves so that the SI result would predominantly contain retrieved surface waves. We select these frequencies based on the power spectrum of the common-source gathers. We then apply SI as described in Section 2.1 by selecting each receiver close to an active source to turn it into a virtual source, as shown by the orange circles in Fig. 2(b). Next, we adaptively subtract the virtual common-source gather from the original active common-source gather which is closest to the virtual source to suppress surface waves. We apply adaptive subtraction by using an estimated matching filter as described in Section 2.2.

It is essential to carefully determine the key parameters for the matching filter: time window, space window and filter length. We select 20 traces for the space window and 0.2 s for the time window, with a filter length of 0.05 s. For the filter length, the goal is to include the complete wave period within it. Taking 20 Hz as the dominant frequency, the corresponding period is 0.05 s, which matches our chosen filter length. For the time window, we aim for a duration several times longer than the period; in this case, we select a time window four times the filter length. Regarding the space window,

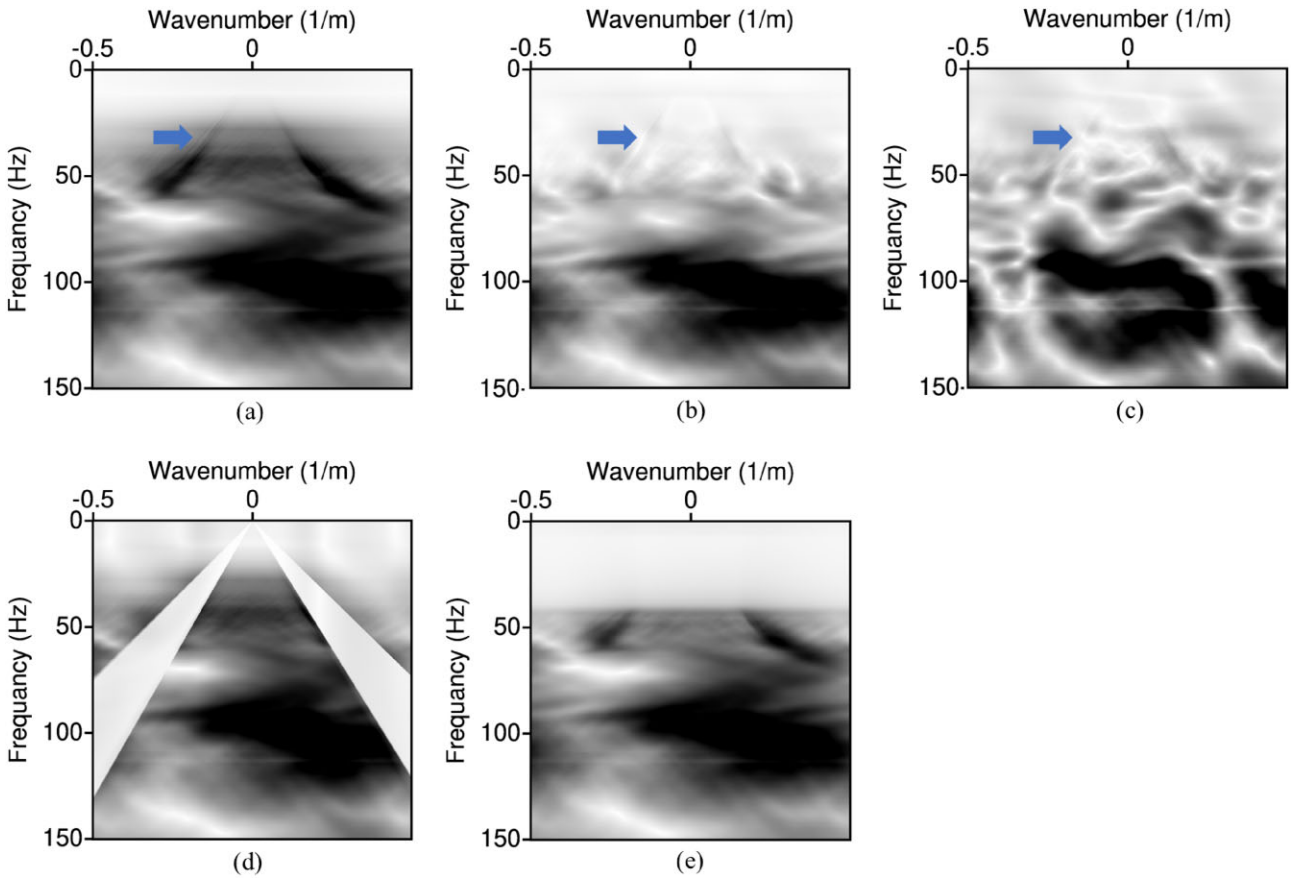

Figure 5. Same as Fig. 4 but in the f-k domain. Arrows point to surface-wave energy in the f-k domain.

we consider the dominant wavelength. For a frequency of 20 Hz and a velocity of 300 m s^{-1}, the wavelength is 15 m. Therefore, it is advisable to choose a space window around this value. Previous studies, such as Balestrini *et al.* (2020), demonstrated that slight variations in the time and space window sizes do not significantly impact the results. Choosing values slightly higher or lower would yield similar performance. We apply the same steps for all virtual sources. Fig. 4(a) shows an example of the original common-source gather in the time domain, while Fig. 4(b) shows the same gather after RISS with one iteration, for an active source located at lateral position 320.5 m.

As discussed in Section 2, we propose to apply the RISS for more than one iteration, which means that we use the data after the first iteration of RISS as input for applying SI. Then, we repeat all steps, that is, band-reject filtering, SI and adaptive subtraction. Note that these steps are shown as 'RISS' in the flowchart in Fig. 3.

Fig. 4(c) shows the same gather as in Figs 4(a) and (b) but after the second iteration of RISS. Comparing these three results, we observe that a large portion of the surface-wave energy is suppressed in Fig. 4(c), as indicated by the white arrows. To demonstrate the effectiveness of the RISS, we additionally applied more conventional approaches for surface-wave suppression, including fk filtering and band-reject filtering between 5 and 40 Hz. The common-source gather for an active source located at a lateral position of 320.5 m after fk filtering and band-reject filtering is shown in Figs 4(d) and (e), respectively. As shown in these figures, both approaches may also remove useful reflection and refraction information from the data and may introduce artefacts.

Figs 5(a)–(e) show the f-k spectra of the common-source gathers illustrated in Figs 4(a)–(e), respectively. The surface-wave energy appears as linear events in the f-k domain, as indicated by the arrows; these linear events are largely suppressed from the data after the RISS with two iterations, as can be noted in Fig. 5(c).

Figs 6 and 7 show another example for a common-source gather for a source located at a lateral position of 430.5 m, where we also observe significant suppression of the surface-wave energy in both the space–time and the f-k domains.

As depicted in Figs 4(c) and 6(c), we successfully suppress the surface waves. However, it appears that some deeper reflections are also suppressed in the process. This shows that applying a simple band-reject filter and relying on having fewer sources in the stationary-phase regions contributing to the retrieval of reflections might not guarantee that the retrieved reflection energy is absent or even weak. To preserve these reflections in the original common-source gathers, we apply a bottom muting to the virtual-common-source gathers retrieved from SI before adaptive subtraction, which we label as 'RISS-muteR' in the flowchart in Fig. 3.

Figs 8(a) and (b) show the unprocessed common-source gather and the common-source gather after applying the RISS. Fig. 8(c) show the common-source gather after applying the RISS using the muted SI results (i.e., RISS-muteR) for an active source located at 320.5 m. In comparison to Fig. 8(b), which shows the same

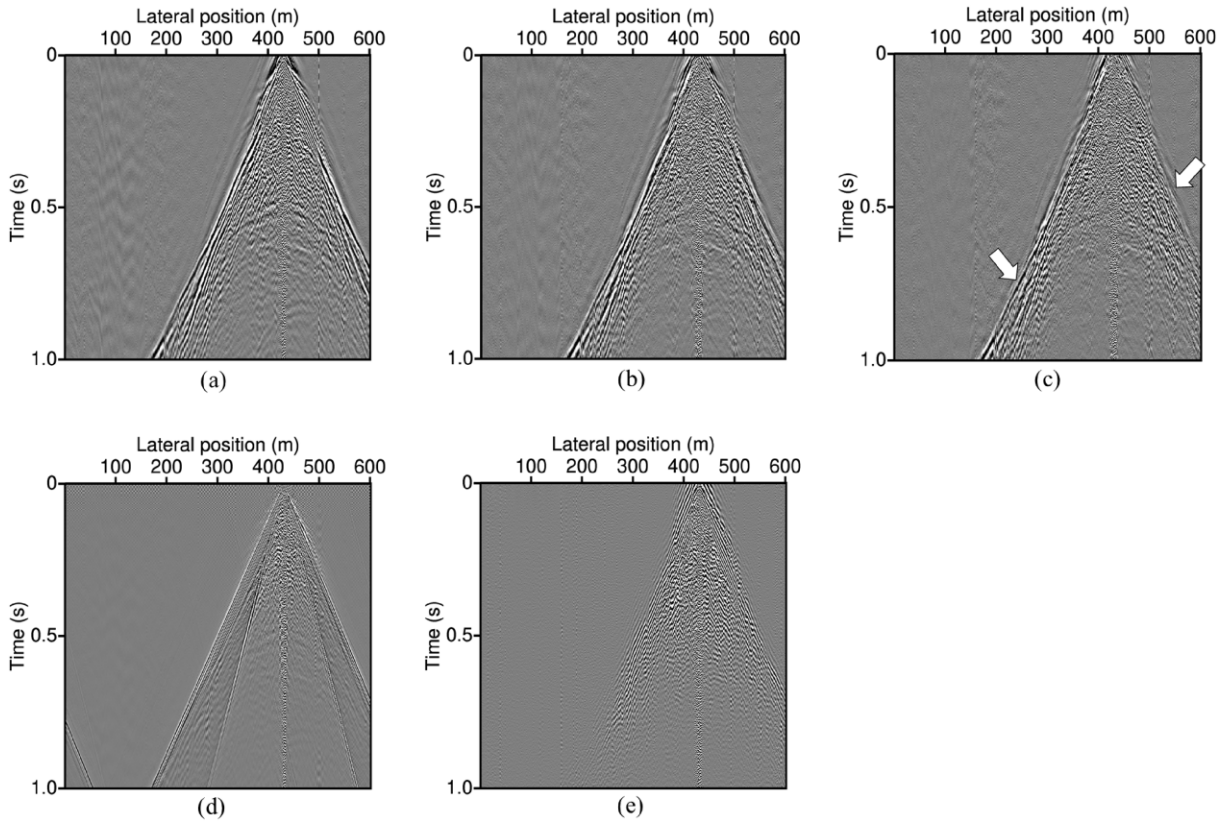

Figure 6. Same as Fig. 4 but for a source located at a lateral position 430.5 m.

common-source gather after RISS, we observe here clearer deeper reflections as marked by the arrows.

By examining the common-source gathers, we observe that it is feasible to suppress some parts of the surface waves through surgical muting, which is a common approach. Therefore, prior to applying the RISS, we can also surgically mute the prominent surface waves. We label this procedure as 'RISS-muteS' in the flowchart in Fig. 3. Fig. 8(d) shows the common-source gather after the RISS-muteS. Although we enhance the resolution of some reflections, we still seem to have some strong surface-wave energy in comparison with the result in Fig. 8(c) as highlighted by the blue ellipses. This observation underscores the fact that by suppressing the surface waves in common-source gathers before the RISS, it becomes challenging to retrieve the surface waves by SI. The suppressed surface waves are highlighted by the green ellipses.

Fig. 9 shows another example for a common-source gather for a source located at a lateral position of 430.5 m.

After the suppression of the surface waves, we apply conventional seismic processing to obtain preliminary unmigrated stacked sections for a better comparison between the result of the RISS and the conventional suppression techniques. A summary of these steps is presented in Table 2. We first apply bandpass filtering, and amplitude correction to compensate for intrinsic attenuation and geometrical spreading, and then automatic gain control (AGC) for balancing the amplitudes along the traces before stacking.

Next, we sort the data into common-midpoint (CMP) gathers (CMP spacing 0.5 m). As expected, the CMP fold increases towards the centre of the line where better illumination is achieved. We then apply normal moveout (NMO) correction using a constant velocity of 350 m s^{-1}, and finally we stack the CMP gathers. The constant velocity of 350 m s^{-1} is selected based on a comparison of the stacked sections with different velocity values, as 350 m s^{-1} velocity yields comparatively better results.

Fig. 10 shows the preliminary unmigrated stacked section between 151.25 and 450.25 m lateral distances for the five approaches to surface-wave suppression as illustrated in Fig. 3: (a) Surgical muting (SS-muteS), (b) RISS with two iterations, (c) the RISS-muteR (same as RISS but using muted SI results), (d) surface-wave suppression using time-muted reflection data set (RISS-muteS) and (e) surface-wave suppression using f-k filtering (SS-fk). Since we know that the most significant influence of the surface waves relates to the shallowest part of the subsurface, we focus our attention on these parts, specifically 400–800 ms.

Fig. 10(a) shows the time section obtained after suppressing the surface waves using surgical muting, as indicated by SS-muteS in the flowchart. We use this figure as a reference because this suppression approach is standard, and experienced data processors generally achieve good results. This result is comparable with results from other studies, for example, that in Kruiver *et al.* (2017).

Fig. 10(b) shows the time section obtained after the second iteration of the RISS. Compared to the reference time section in Fig. 10(a), the surface-wave suppression is similar between the two sections. However, it is evident that some expected reflectors are also suppressed, as indicated by the red and green arrows. This observation highlights that using a simple band-reject filter may not guarantee that the retrieved reflection energy is either absent or significantly weakened in the results of SI.

To address this issue, we use the RISS-muteR as explained above. Fig. 10(c) illustrates the time section obtained after the application of this technique. In comparison with the reference in

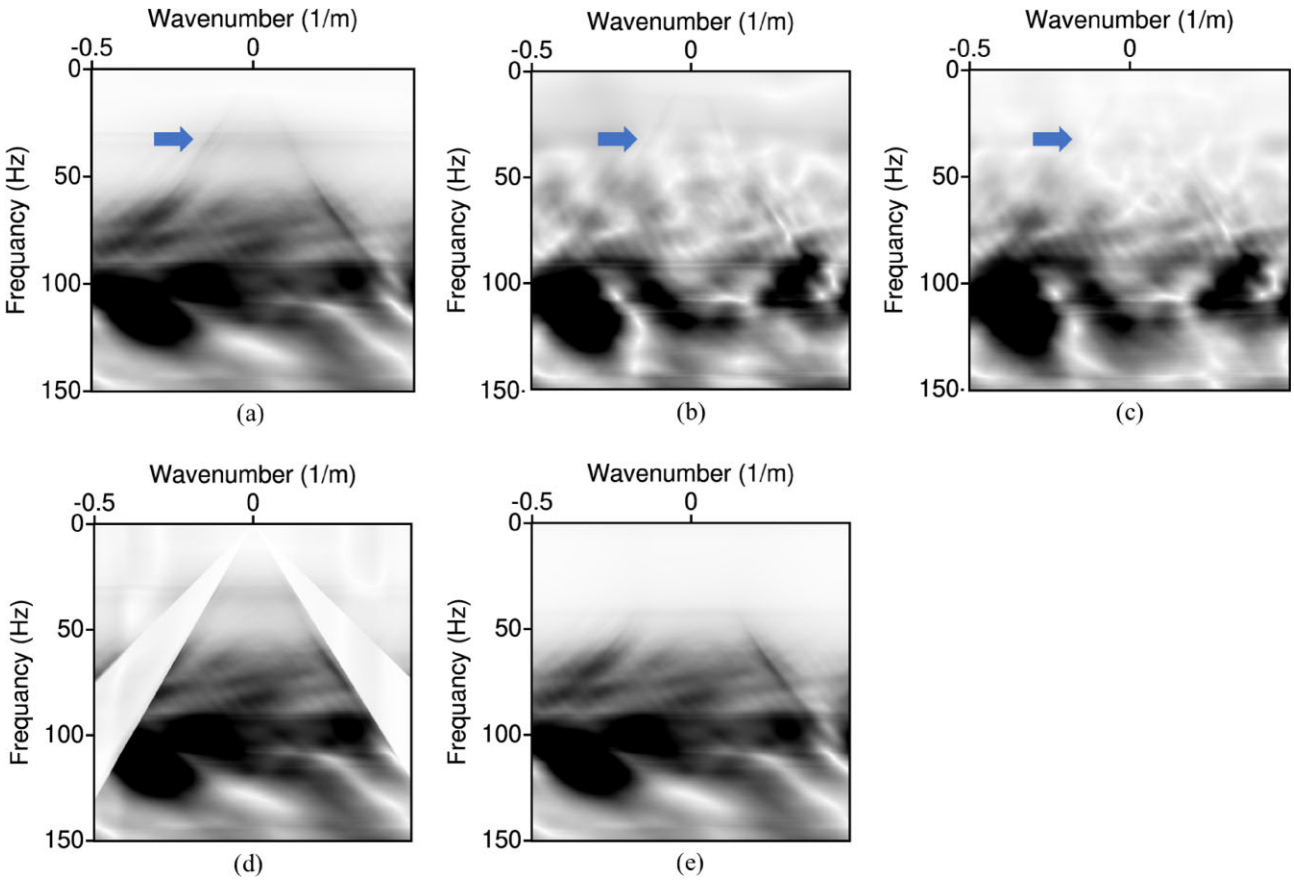

Figure 7. Same as Fig. 5 but for a source located at a lateral position 430.5 m.

Fig. 10(a), we retrieve all reflectors, as indicated by the orange, red and green arrows, and some dome-like structures are now interpretable as highlighted by the red curves and the event marked by the cyan arrow. This improvement is due to suppressing those parts of surface waves which cannot be suppressed just by using surgical muting.

Fig. 10(d) shows the time section after applying RISS-muteS. Comparing this image to the images in Figs 10(a) and (c), we see that the lateral continuity of the reflectors is worse, for example, inside the blue ellipse, while the general character on the left part of the image has changed, the wavefield becoming enriched with lower frequencies, which might point to the presence of left-over dominant surface-wave energy.

Fig. 10(e) shows the time section obtained after suppression of the surface waves by f-k filtering (SS-fk). F-k filtering is commonly used for surface-wave suppression. Comparing the image in Figs 10(e) with the images in Figs 10(a) and (c), we see that the result in Fig. 10(e) is generally of good quality too. Although no ground truth is available, certain observations can be made. The event at 600 ms (green arrow) lies comfortably inside the window of the f-k filter and is therefore well-preserved; it is also clearly visible in the RISS result (Fig. 10c). The continuity of this event around CMP 251 remains uncertain: it appears more continuous in the f-k result but less continuous in the RISS result. In general, the result after f-k filtering appears to be better than after RISS close to the left and right ends of the seismic line, and especially close to the left end. This difference reflects limitations of SI, a component of RISS, which requires sufficient sources on both sides of the receivers. For our data set, the number of sources at both ends of the line is limited due to the acquisition geometry (e.g. at position 150 only right-side sources are available). In our stacked sections, the CMP-fold is maximum and constant in the lateral range 225–355 m; outside this range the stack-fold gradually decreases towards the ends of the seismic line. This reduce the quality of the SI results near the edges of the survey line. For a correct comparison, one needs same illumination (same source distribution on both sides of the receiver) for both f-k filtering and RISS. In the central part of our seismic line, it can be argued that RISS possibly performs better than f-k filtering. For instance, the event indicated by the cyan arrow and line in Fig. 10 appears in Fig. 10(c) as a clear syncline structure, while in the f-k filtering result (Fig. 10e) the definition of the structure is less clear. As this event falls in the blue-highlighted area in Fig. 10(e), one might erroneously interpret it as a faulted structure while in fact it might be largely an artefact of f-k filtering. The dome-like events marked by the red lines in Fig. 10(c) correspond to clear reflections seen in the common-source gathers, and are therefore also highlighted in the stacked section. These events appear more clearly in the RISS result (Fig. 10c) than in the f-k filtering result (Fig. 10e). The similar dome-like events at two-way time ∼400 ms are interpretable in the f-k result but they are also visible in the stacked sections in Figs 10(a) and (c), albeit in Fig. 10(c) the dome-like event at ∼310 m is rather unclear. Again, without ground truth it is not possible to confirm which feature is real. However, our findings suggest that the RISS result is at least as good at the f-k filtering result.

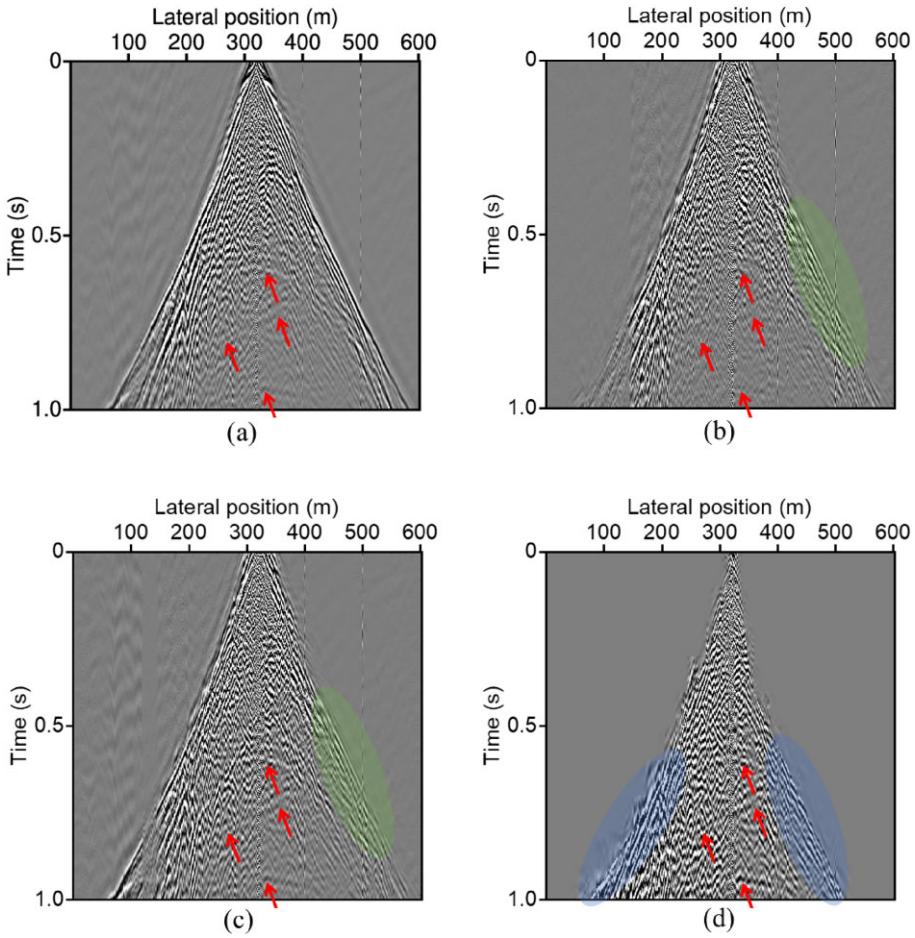

Figure 8. (a) A common-source gather for a source located at lateral position 320.5 m, (b) same common-source gather after the RISS, (c) same common-source gather after the RISS-muteR, (d) same common-source gather after the RISS-muteS.The arrows point to enhanced reflections, while the blue ellipses highlight parts of the surface waves, the green ellipses highlight parts of the suppressed surface waves.

5 DISCUSSION

We presented a comparison of different approaches for surface-wave suppression applied to a land seismic data set acquired in Scheemda, Groningen province: surgical muting, f-k filtering, the RISS, the RISS-muteR and the RISS-muteS.

From a comparison of the unmigrated time sections, we found that surgical muting seems convenient for removing surface waves in our data set. However, this approach does not adequately remove the surface-wave energy, as surface waves overlap with useful reflections and scattered arrivals. Additionally, weak reflections and scattered arrivals covered by surface waves might also be muted, as demonstrated earlier by Konstantaki *et al.* (2015). Another common approach to suppress the surface waves involves f-k filtering. RISS provides an alternative, data-driven approach that provided results at least as good as those from f-k filtering. RISS is particularly useful when the surface-wave and *S*-wave velocities are similar, and thus, where the f-k filtering runs the risk of removing parts of the reflection signals. Unlike f-k filtering, which is an array-based approach which requires dense placement of receivers to avoid aliasing, RISS can work with as few as two receivers, as SI by cross-correlation is essentially a two-station method. On the other hand, RISS depends on the availability of enough sources for stacking. It is also possible to turn our sources into virtual receivers and follow the same procedure in the case of insufficients source albeit this would require having sufficient receivers for stacking.

By comparing three approaches for the RISS methodology, we found that the RISS using muted deeper reflections after retrieving the surface waves with SI yields the best results. RISS with two iterations was sufficient to achieve the desired results for our data set. However, more than two iterations can be needed for other data sets.

For implementation of RISS, we must determine the time, the spatial window and the filter length. Using a few well-known parameters from the data, such as the dominant wavelength, we can define all necessary parameters for RISS. If the parameters are not chosen appropriately, the results can be poor and show limited suppression, but RISS will not create artefacts and is, thus, not highly sensitive to all such parameter settings, as illustrated in Balestrini *et al.* (2020). In our study, we used the same parameters for both iterations, but it might be useful to change these parameters in each iteration.

As described in the methodology section, we utilized the field data set with surface waves for each active source as a reference, and for the virtual sources, the surface waves were retrieved using SI. In our study, we created the virtual sources at the receiver

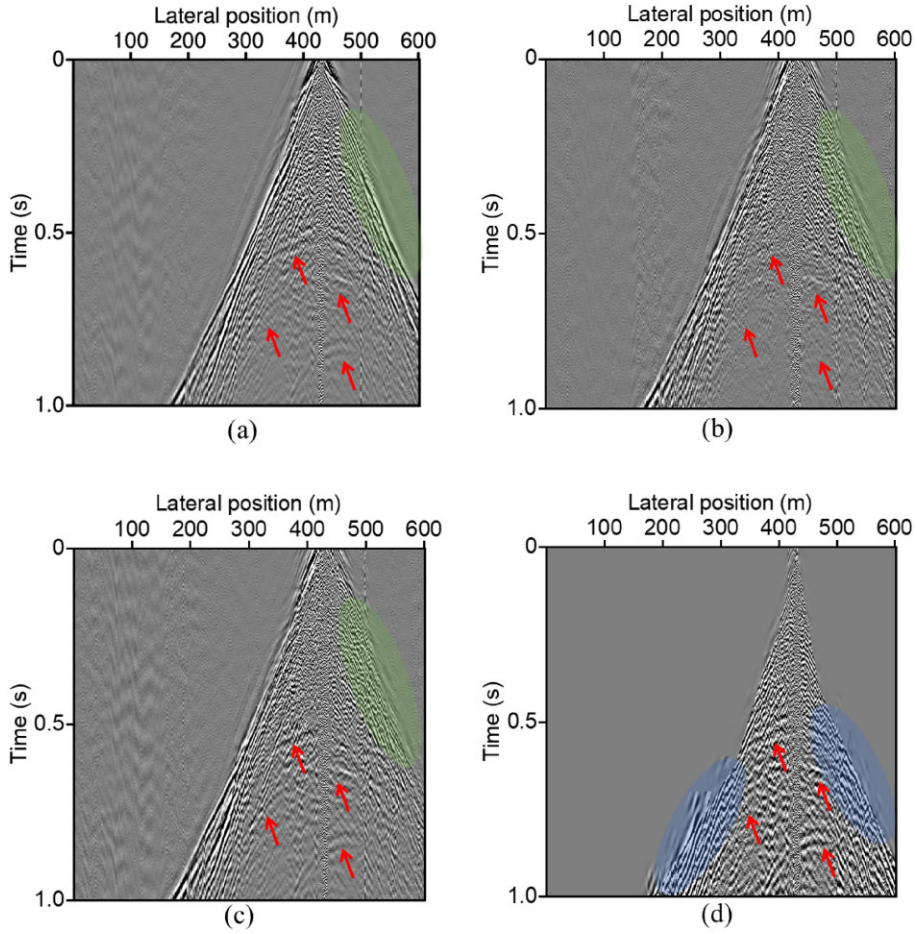

Figure 9. Same as Fig. 8 but for a source located at a lateral position 430.5 m.

Table 2. Summary of seismic processing steps.

Step	Instruction
1	Band-pass filtering 30–100 Hz
2	Amplitude corrections
3	Automatic gain control (AGC)
4	Time muting
5	Normal moveout (NMO) correction
6	Common midpoint/ensemble stack

locations, which are positioned at 0.5 m from the active sources; this provides an appropriate data set for applying this technique. However, using virtual sources located at greater distances from the active sources may result in incorrect estimations of the surface waves using SI. Therefore, we recommend using sources and receivers in close proximity of each other to ensure the accuracy of RISS.

In general, other studies, such as Halliday & Curtis (2008), have demonstrated that successfully recovering the higher-mode surface waves using only surface sources is challenging. Consequently, modal separation may be a crucial step before applying SI to ensure accurate kinematic retrieval and effective suppression of the higher modes with minimal error. RISS, however, can facilitate the suppression of higher modes. During each iteration, the strongest surface-wave mode is retrieved and adaptively suppressed, effectively functioning as step-wise modal separation, as discussed in Appendix A by using a numerically modelled data set.

We showed that the RISS technique can be effective for enhancing the resolution of seismic reflection events in common-source gathers and in stacked unmigrated time sections. To further investigate the applicability of this technique, we used data after RISS also for the Marchenko-based isolation technique, which showed enhanced reflections with greater clarity in the stacked sections. These results and more details can be found in Appendix B.

6 CONCLUSION

We proposed a recursive application of seismic interferometry (SI) for surface-wave suppression. We showcased our technique using a 2-D reflection data set acquired in Scheemda, Groningen province, the Netherlands. We applied SI to retrieve dominant surface waves between receivers while minimizing the retrieved reflection energy. The retrieved dominant surface waves are then adaptively subtracted from the original data. We showed that applying these two steps two times, that is, recursively, resulted in a fully data-driven effective suppression of the surface waves.

We compared stacked sections obtained through the recursive interferometric surface-wave suppresion (RISS) with stacked sections where the surface waves were suppressed using frecuency-wavenumber (f-k) filtering and surgical muting. We found that the obtained time section after the second iteration of RISS yielded better results than the surgical muting in terms of clearer and more continuous reflections and the RISS result is at least as good at the f-k filtering result. The best RISS result was the one in which the

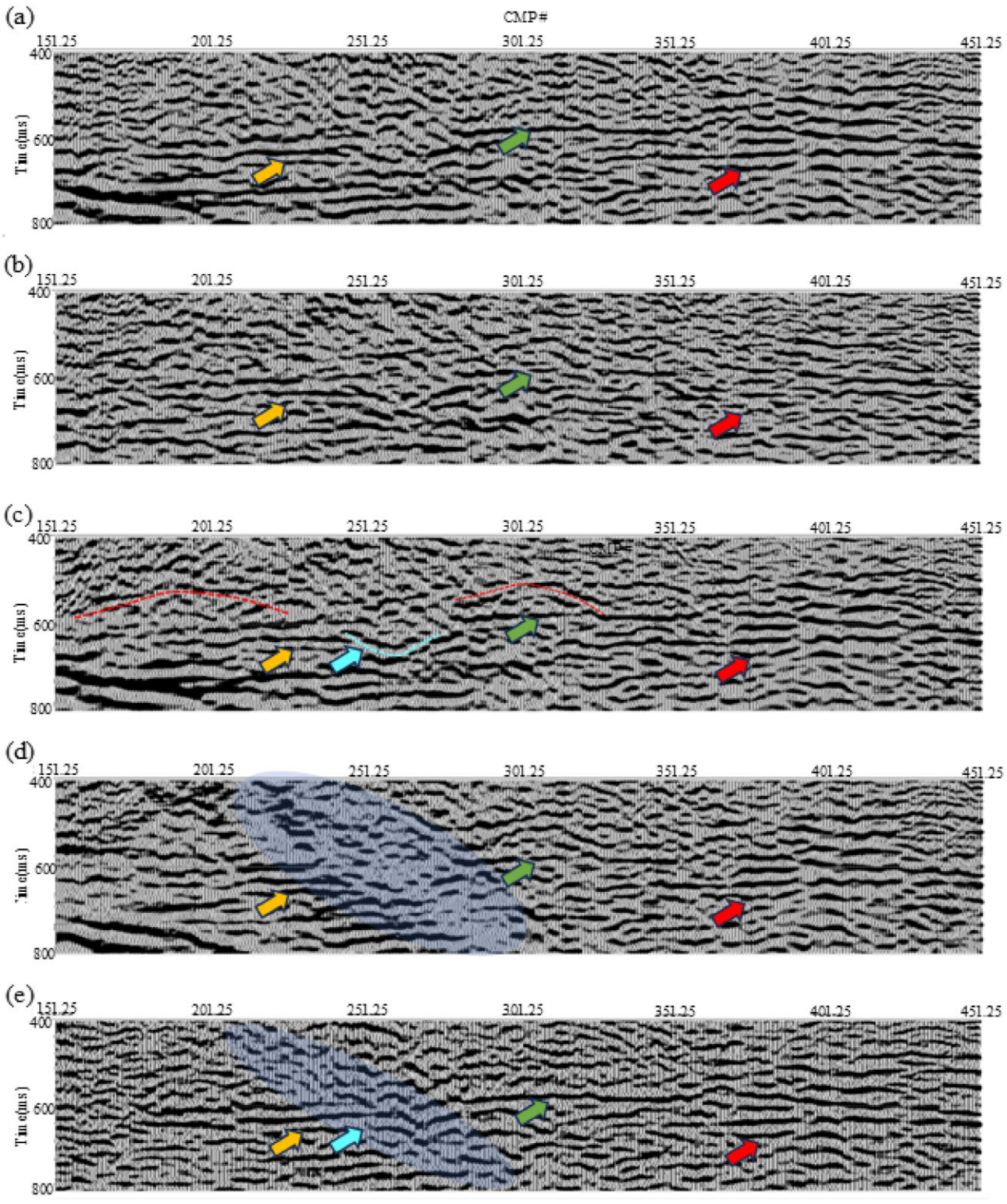

Figure 10. Preliminary unmigrated stacked section (400–800 ms) using a constant velocity of 350 m s^{-1}: (a) using the reflection data set after surgical muting of surface waves ('SS-muteS'), (b) after the second iteration of the RISS, (c) after the RISS using the muted SI results (RISS-muteR), (d) using the data as in (a) but after the RISS ('RISS-muteS'), (e) after f-k filtering ('SS-fk'). The coloured arrows point to strong reflectors and the blue ellipses highlight artefacts.

retrieved reflection energy after SI was minimized by bottom muting before the application of adaptive subtraction. The presented RISS approach can be effective for enhancing the resolution of the seismic reflection events for subsurface investigations.

ACKNOWLEDGMENTS

We acknowledge the use of computational resources provided by the DelftBlue supercomputer at the Delft High Performance

Computing Centre (https://www.tudelft.nl/dhpc) and thank Seismic Mechatronics for allowing us to use their vibrator source during fieldwork (https://seismic-mechatronics.com/).

This research is funded by NWO Science domain (NWO-ENW), project DEEP.NL.2018.048 and the reflection data set was acquired by funding from the European Research Council (ERC) under the European Union's Horizon 2020 research and innovation programme (Grant Agreement No. 742703) and OYO Corporation, Japan: OYO-TUD Research Collaboration (Project code C25B74).

DATA AVAILABILITY

The field reflection data set used in this study is available in the 4TU.ResearchData repository at https://doi.org/10.4121/a8553b7e-82ae-4e9b-bc54-2a6b9ca6063c.

The codes are also accessible in the 4TU.ResearchData repository at https://doi.org/10.4121/6271c7d3-f931-49e9-b2b0-2d05eef7d3ae.

REFERENCES

Alá'i, R. & Verschuur, D., 2003. Simultaneous adaptive least-squares subtraction of multiples, in *65th EAGE Conference and Exhibition,* European Association of Geoscientists and Engineers, pp. 1–4.

Balestrini, F., Draganov, D., Malehmir, A., Marsden, P. & Ghose, R., 2020. Improved target illumination at Ludvika mines of Sweden through seismic-interferometric surface-wave suppression, *Geophys. Prospect.,* **68**(1), 200–213..

Campillo, M. & Paul, A., 2003. Long-range correlations in the diffuse seismic coda, *Science,* **299**(5606), 547–549..

Curtis, A., Gerstoft, P., Sato, H., Snieder, R. & Wapenaar, K., 2006. Seismic interferometry—turning noise into signal, *Leading Edge,* **25**(9), 1082–1092..

Dong, S., He, R. & Schuster, G.T., 2006. Interferometric prediction and least squares subtraction of surface waves, *SEG Technical Program Expanded Abstracts 2006,* 2783–2786. doi: 10.1190/1.2370102

Halliday, D. & Curtis, A., 2008. Seismic interferometry, surface waves and source distribution, *Geophys. J. Int.,* **175**(3), 1067–1087..

Halliday, D., Curtis, A., Vermeer, P., Strobbia, C., Glushchenko, A., van Manen, D.J. & Robertsson, J.O., 2010. Interferometric ground-roll removal: Attenuation of scattered surface waves in single-sensor data, *Geophysics,* **75**(2), SA15–SA25..

Konstantaki, L., Draganov, D., Ghose, R. & Heimovaara, T., 2015. Seismic interferometry as a tool for improved imaging of the heterogeneities in the body of a landfill, *J. Appl. Geophys.,* **122,** 28–39..

Kruiver, P.P. *et al.*, 2017. An integrated shear-wave velocity model for the Groningen gas field, the Netherlands, *Bull. Earthq. Eng.,* **15**(9), 3555–3580.

Larose, E. *et al.*, 2006. Correlation of random wave fields: An interdisciplinary review, *Geophysics,* **71**(4), SI11–SI21..

Liu, J., Draganov, D. & Ghose, R., 2018. Seismic interferometry facilitating the imaging of shallow shear-wave reflections hidden beneath surface waves, *Near Surf. Geophys.,* **16**(3), 372–382..

Lobkis, O.I. & Weaver, R.L., 2001. On the emergence of the Green's function in the correlations of a diffuse field, *J. acoust. Soc. Am.,* **110**(6), 3011–3017.

Muntendam-Bos, A.G., Hoedeman, G., Polychronopoulou, K., Draganov, D., Weemstra, C., van der Zee, W., Bakker, R.R. & Roest, H., 2022. An overview of induced seismicity in the Netherlands, *Geol. Mijnbouw/Netherlands J. Geosci.,* **101**(2), 1–20.

Noorlandt, R., Drijkoningen, G., Dams, J. & Jenneskens, R., 2015. A seismic vertical vibrator driven by linear synchronous motors, *Geophysics,* **80**(2), EN57–EN67..

Yilmaz, Öz, 2001. *Seismic Data Analysis,* Society of Exploration Geophysicists.

Schuster, G.T. & Zhou, M., 2006. A theoretical overview of model-based and correlation-based redatuming methods, *Geophysics,* **71**(4), SI103–SI110..

Shirmohammadi, F., Draganov, D., van IJsseldijk, J., Ghose, R., Thorbecke, J., Verschuur, E. & Wapenaar, K., 2025. Application of Marchenko-based isolation to a land s-wave seismic data set, *Geophys. Prospect.,* **73,** doi: 10.1111/1365-2478.70064

Slob, E., Wapenaar, K., Broggini, F. & Snieder, R., 2014. Seismic reflector imaging using internal multiples with Marchenko-type equations, *Geophysics,* **79**(2), S63–S76..

Thorbecke, J.W. & Draganov, D., 2011. Finite-difference modeling experiments for seismic interferometry, *Geophysics,* **76**(6), H1–H18..

van IJsseldijk, J., van der Neut, J., Thorbecke, J. & Wapenaar, K., 2023. Extracting small time-lapse traveltime changes in a reservoir using primaries and internal multiples after Marchenko-based target zone isolation, *Geophysics,* **88**(2), R135–R143..

van IJsseldijk, J., Brackenhoff, J., Thorbecke, J. & Wapenaar, K., 2024. Time-lapse applications of the Marchenko method on the Troll field, *Geophys. Prospect.,* **72**(3), 1026–1036..

van Manen, D.J., Curtis, A. & Robertsson, J.O., 2006. Interferometric modeling of wave propagation in inhomogeneous elastic media using time reversal and reciprocity, *Geophysics,* **71**(4), SI47–SI60..

Verschuur, D., 2013. *Seismic Multiple Removal Techniques - Past, Present and Future,* European Association of Geoscientists and Engineers (EAGE).

Verschuur, D.J., Berkhout, A.J. & Wapenaar, C.P.A., 1992. Adaptive surface-related multiple elimination, *Geophysics,* **57**(9), 1166–1177..

Wapenaar, K. & Fokkema, J., 2006. Green's function representations for seismic interferometry, *Geophysics,* **71**(4), SI33–SI46..

Wapenaar, K. & van IJsseldijk, J., 2021. Employing internal multiples in time-lapse seismic monitoring, using the Marchenko method, in *82nd EAGE Conference and Exhibition 2021,* European Association of Geoscientists and Engineers, pp. 1–5.

Wapenaar, K., Dillen, M.W.P. & Fokkema, J., 2001. Reciprocity theorems for electromagnetic or acoustic one-way wave fields in dissipative inhomogeneous media, *Radio Sci.,* **36**(5), 851–863.

Wapenaar, K., Thorbecke, J., van der Neut, J., Broggini, F., Slob, E. & Snieder, R., 2014. Marchenko imaging, *Geophysics,* **79**(3), WA39–WA57..

APPENDIX A: SUPPRESSION OF DIFFERENT MODES OF SURFACE WAVES USING A NUMERICALLY MODELLED DATA SET

To investigate the possibility of suppressing higher modes of surface waves using RISS, we use numerical modelling based on the velocity model presented in fig. 3 of Halliday & Curtis (2008), which has been summarized in Table A1. We use a finite-difference modelling code (Thorbecke & Draganov 2011) in 2-D acoustic mode with a rigid boundary at the surface to generate the full seismic data set, including reflections and guided waves. Based on the analogy between 2-D acoustic waves in a fluid and 2-D *SH* waves in a solid (Wapenaar *et al.* 2001), this approach is equivalent to generating *SH* waves including Love waves, in the elastic mode with a free-surface boundary at the surface. The fixed receivers are placed from 100 m to 400 m with 1 m spacing, and the sources are placed from 50.25 to 450.25 m with 2 m spacing.

Fig. A1(a) shows a common-source gather in the time domain for a source located at 100.25 m, while Fig. A1(c) shows the same common-source gather in the f-k domain. In this figure, the fundamental-mode surface wave is indicated by a blue arrow, while the first higher mode is indicated by a purple arrow.

First, we apply f-k filtering to the data set in order to provide a meaningful comparison with the RISS method. Fig. A2(a) presents

Table A1. Velocity and density model used for numerical modelling (Halliday & Curtis 2008).

Depth (m)	V_s (m s^{-1})	Density (kg m^{-3})
0–1	101	1400
1–2	126	1460
2–4	127	1470
4–6	146	1520
6–8	172	1590
8–12	184	1610
12–20	200	1650
20–30	232	1710
30-	307	1840

the common-source gather after f-k filtering, while Fig. A2(c) displays the corresponding gather in the f-k domain. To understand the result of the f-k-filtering process, we generate a second synthetic data set using finite-difference modelling (Thorbecke & Draganov 2011) in 2-D acoustic mode, but using *S*-wave velocities and densities from Table A1, with a reflection-free surface condition. Under these conditions, and the aforementioned analogy between acoustic and *SH* waves, the data set contains only *S* body waves, including direct waves, reflections, refractions. The modelled common-source gather is shown in Fig. A1(b), and its representation in the f-k domain is provided in Fig. A1(d). In Fig. A1(d), the locations of the fundamental and higher modes of surface waves are indicated using the colour coding from Fig. A1(c), highlighting their positions relative to the pure *S* body-wave events. The results clearly show that parts of the surface waves, particularly the higher mode, overlap with *S* body-wave events. Consequently, applying f-k filtering can lead to the unintended removal of valuable information, as demonstrated in Fig. A2(d). Additionally, f-k filtering may introduce artefacts into the data, as indicated by the arrows in Fig. A2(a).

We also apply RISS to this data set. Fig. A3(a) shows the common-source gather after the first iteration, and Fig. A3(d) shows the common-source gather after the second iteration. Figs A3(b) and (e) show the same common-source gathers in the f-k domain after the first and second iterations, respectively. To better evaluate the suppression of the different surface-wave modes, the results of SI before adaptive subtraction are shown in Figs A3(c) and (f), after the first and second iterations, respectively.

As we can see in Figs A3(a) and (d), the strong surface waves have been effectively suppressed. However, it is challenging to discriminate between the fundamental- and the higher-mode surface waves in the space–time domain. Nevertheless, it is clear from the common-source gathers in the f-k domain that we effectively estimate mainly the fundamental mode in the result of SI after the first iteration as shown in Fig. A3(c). As a result of the subtraction, we mainly remove the fundamental mode in the first iteration, while the higher mode still remains (Fig. A3b). In the second iteration, we further estimate the remaining part of the fundamental mode but now also the higher mode, as shown in the result of SI in Fig. A3(f). As a result of the subtraction, we suppress further the fundamental-mode and, importantly, also the higher-mode surface wave, as shown in Fig. A3(e).

In conclusion, we demonstrate that during the two iterations, the strongest part of the surface-wave energy is retrieved and adaptively

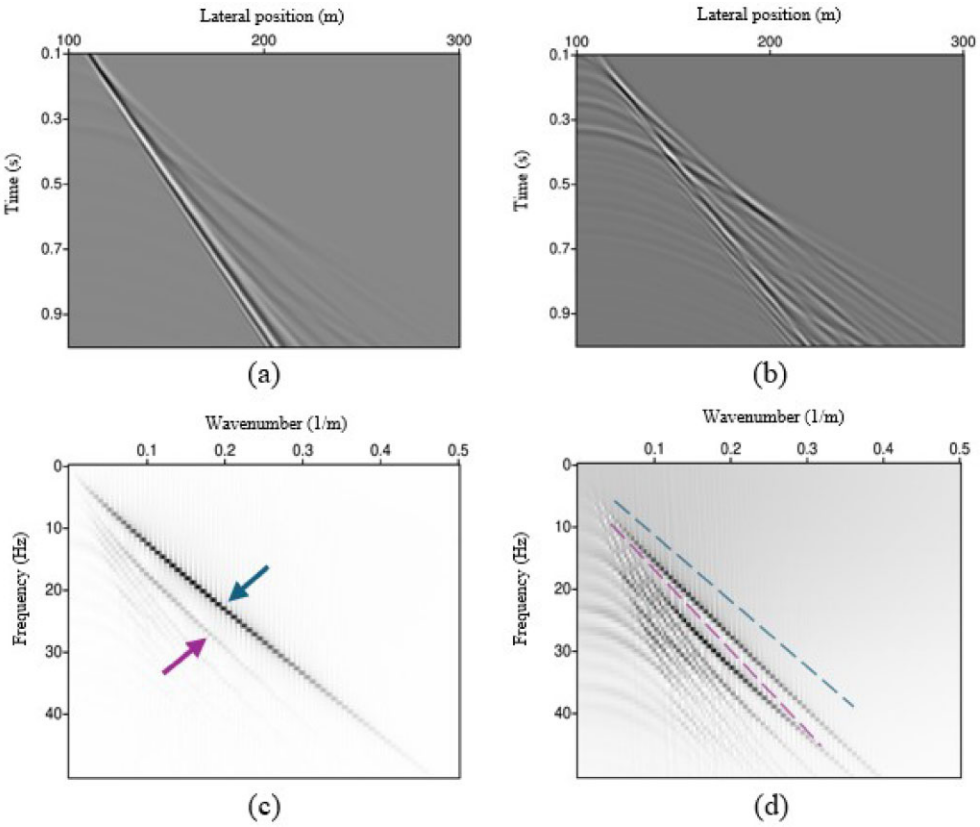

Figure A1. (a) A common-source gather for a source located at lateral position 100.25 m modelled using acoustic modelling with a rigid boundary at the surface. (b) The common-source gather generated by acoustic modelling with a reflection-free surface at the surface. (c) The common-source gather in (a) in the f-k domain. (d) The common source gather in (b) in the f-k domain. The blue arrow (dashed line) indicates the fundamental-mode surface wave, the purple arrow (dashed line) indicates the higher mode surface wave.

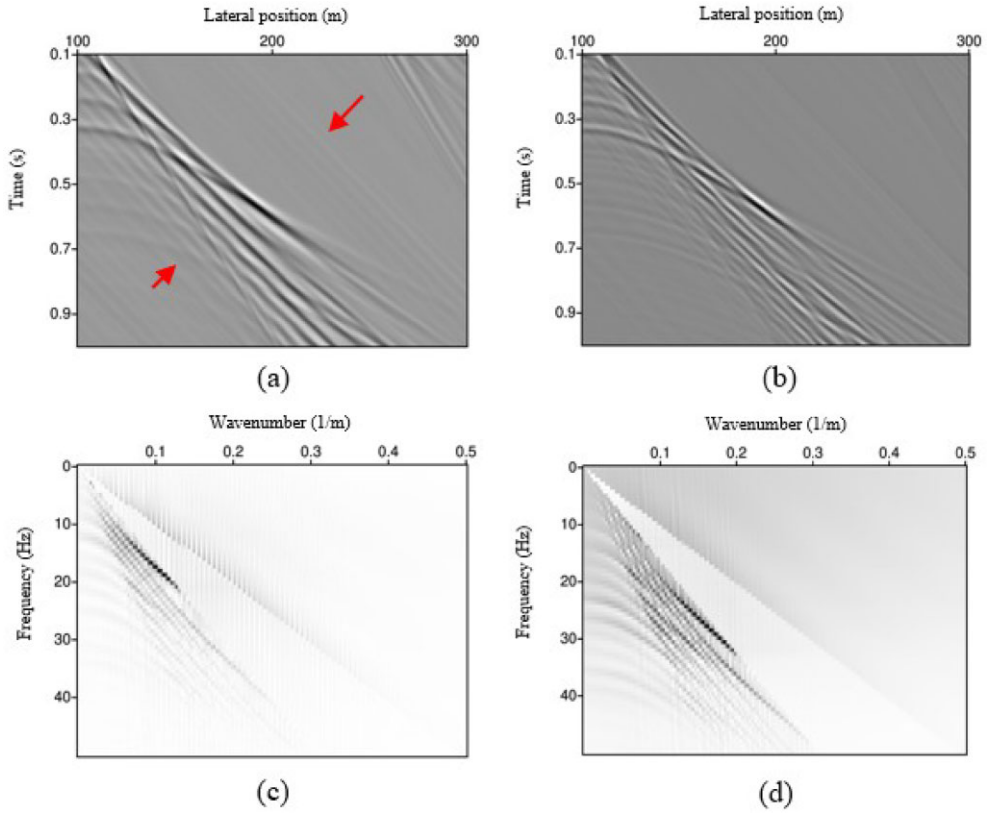

Figure A2. Same as Fig. A1 but after f-k filtering. The arrows indicate artefacts after the f-k filtering.

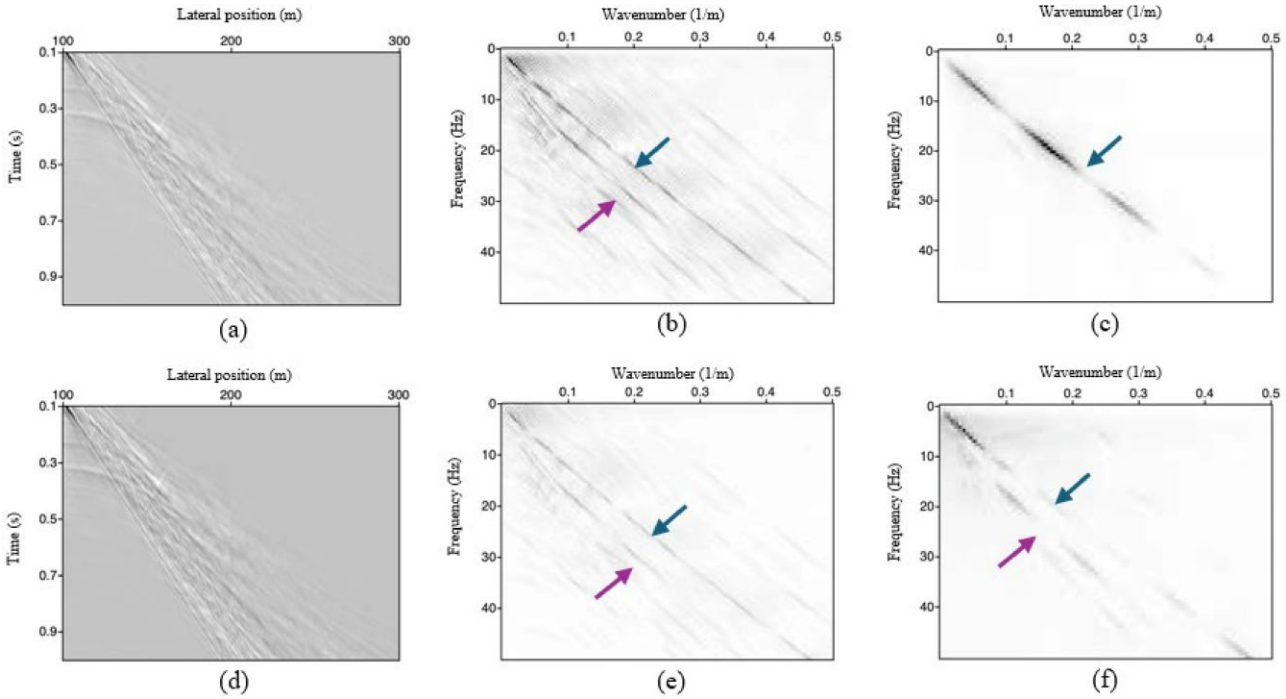

Figure A3. (a) A common-source gather after the first iteration of the RISS. (b) The common-source gather from (a) in the f-k domain. (c) Virtual common-source gather (i.e. result of SI before adaptive subtraction) in the f-k domain for the source located at lateral position 100 m. (d), (e) and (f): Same as (a), (b) and (c), respectively, but for the second iteration. The blue arrow points to the fundamental-mode surface wave, while the purple arrow highlights the higher mode surface wave.

suppressed, effectively achieving step-wise modal separation. This provides the possibility of suppressing the fundamental- and the higher-modes surface waves. It is important to note that, in this example, we use a simple subsurface model with a clear separation between the surface-wave modes. However, in the field data set in Appendix B, it is not as straightforward to determine which part of the surface waves is suppressed in each iteration. Nonetheless, based on this numerical modelling, it is reasonable to assume that the iterative procedure can suppress the fundamental mode and (some of) the higher-order modes.

APPENDIX B: APPLICATION OF RISS FOR THE MARCHENKO-BASED ISOLATION METHOD

To demonstrate the applicability of using SI for surface-wave suppression in the imaging of the shallow subsurface, we further investigate its use for the Marchenko-based isolation method (Wapenaar & van IJsseldijk 2021; van IJsseldijk *et al.* 2023). The Marchenko method can estimate Green's functions between the Earth's surface and arbitrary locations in the subsurface. These Green's functions are used to redatum wavefields to a deeper level in the subsurface (Slob *et al.* 2014; Wapenaar *et al.* 2014). The Marchenko method can also be used to isolate the response of a specific layer or a package of layers, free from the influence of the overburden and the underburden. The complete derivation of Marchenko-based isolation is beyond the scope of this paper; however, a detailed description can be found in van IJsseldijk *et al.* (2023, 2024). Moreover, a complete description of the application of Marchenko-based isolation on the field data set used in this study can be found in Shirmohammadi *et al.* (2025).

We use the Marchenko-based isolation method to eliminate the overburden and the underburden, and isolate the reflection from the target layer between 30 and 270 m using the data after surgical muting of surface waves and the data after RISS-muteR. Fig. B1(a) shows the stacked section using the regular reflection response after suppression of the surface waves using surgical muting, while Figs B1(b) and (c) show the stacked section using the reflection response after Marchenko-based isolation for overburden and underburden removal, using surgical muting for surface-wave suppression and RISS-muteR, respectively. Note that we show the image plots of the section rather than the wiggle representations in Fig. 10.

A comparison of these stacked sections in Fig. B1 suggests the potential elimination of the internal multiples originating from the overburden, down to 30 m using the Marchenko-based isolation. The shallow reflectors appear clearer and more continuous, as indicated by the colour-coded arrows. But what we want to draw attention to is the effect of surface-wave suppression on these results. We observe enhanced reflections with greater clarity in the stacked sections after RISS-muteR (Fig. B1c), as exemplified by the events indicated by the white and green arrows. Moreover, there are fewer artefacts, likely from the surface waves, as indicated by the black ellipse.

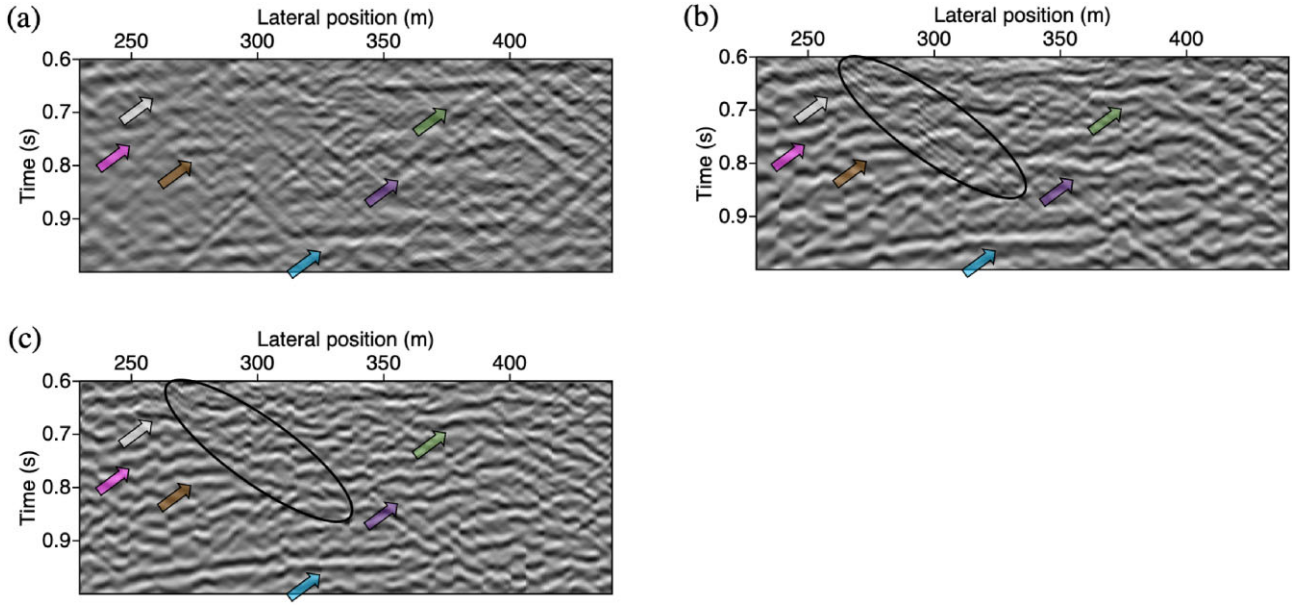

Figure B1. Stacked sections, zoomed in between 0.6 and 1.0 s, obtained using (a) the regular reflection response after surgical muting of the surface waves, (b) the reflection response after Marchenko-based isolation for overburden and underburden removal after surgical muting of the surface waves and (c) similar to (b) but using data after surface-wave suppression with RISS-muteR instead of surgical muting. The colour-coded arrows indicate reflectors. The black ellipse highlights potential artefacts from the surface waves that are suppressed in (c).